# A Tightly Coupled LiDAR/IMU/GNSS Navigation System Based on GNSS NLOS Correction

Zhen Zhang<sup>1</sup>, Paipai Wu<sup>1</sup>, Yangzi Cong<sup>1\*</sup>, Wenpeng Zong<sup>2</sup>, Wenfeng Nie<sup>1</sup>, Tianhe Xu<sup>1</sup>

<sup>1</sup> School of Space Science and Technology, ShanDong University, Weihai, China; <sup>2</sup> Xi'an Institute of Surveying and Mapping, Xi'an, China.

**Keywords:** LiDAR, IMU, GNSS, NLOS, Multi-Source Fusion.

### **Abstract**

With the rapid development of artificial intelligence and autonomous driving technology, the demand for high-precision, high-reliability and continuous positioning services has become increasingly obvious. However, in complex urban environments, GNSS signals are prone to the non-line-of-sight (NLOS) propagation effect, which leads to systematically large observation errors and then significantly reduces the navigation accuracy. To address this, we propose a tightly coupled LiDAR/IMU/GNSS navigation framework based on raw GNSS observations. Additionally, we incorporate LiDAR point cloud data to develop a NLOS satellite detection and correction module. This module constructs a 3D LiDAR point cloud map of the sensor's surroundings and identifies NLOS signals by analysing the geometric relationships between the sensor, satellites, and the environmental map. Furthermore, reflection points from the surrounding environment are extracted and utilized for NLOS correction. The results of two groups of independent experiments show that the system positioning error after NLOS correction is reduced by 16.15%. Compared with the conventional integration system that adopts pseudorange difference information, the proposed framework achieves a 32.57% improvement in navigation accuracy under complex urban scenarios, demonstrating its effectiveness.

#### 1. Introduction

The rapid progress of technologies such as artificial intelligence and autonomous driving has led to a significant increase in the demand for high-precision navigation and positioning services. In the domains of autonomous driving and intelligent robotics, continuous and reliable position information is essential for critical tasks, including decision-making, control, and path planning (S. Kuutti et al., 2018; Vivacqua et al., 2017). Consequently, the development of a high-precision and highly robust navigation system is of paramount importance.

As one of the most widely utilized navigation technologies, Inertial Navigation Systems (INS) can autonomously estimate a carrier's velocity, position, and attitude based solely on the output of an Inertial Measurement Unit (IMU). However, the inherent error accumulation in IMU measurements leads to a progressive degradation of navigation accuracy over time (Garg et al., 1978; Pinana-Diaz et al., 2011). Light Detection and Ranging (LiDAR), as a high-precision ranging sensor, enables both environmental perception and autonomous positioning. In complex outdoor environments, LiDAR provides stable distance measurements due to its strong anti-interference capability. Notably, LiDAR Odometry And Mapping (LOAM) methods (Zhang and Singh, 2014; Zhang and Singh, 2017), along with LeGO-LOAM (Shan and Englot, 2018), utilize IMU-derived data as a priori information for LiDAR frame-toframe matching, thereby improving accuracy. Nevertheless, error accumulation remains an unavoidable challenge in longrange navigation tasks (Zhou, 2022). Global Navigation Satellite System (GNSS), a well-established absolute positioning technology, has been widely applied in aviation, marine navigation, and geological exploration, among other fields. Its primary advantages include extensive coverage and high positioning accuracy (Yang et al., 2011; Yang et al., 2019). However, in urban canyons, tunnels, and dense high-rise

environments, GNSS signals are highly susceptible to occlusion and multipath effects, leading to significant positioning errors and reduced reliability in such complex settings.

Although different types of sensors offer unique advantages, a single sensor alone is often insufficient to meet the positioning requirements in complex and dynamic environments. Multisensor fusion, which leverages the strengths of each sensor while mitigating their inherent limitations, has proven to be an effective approach for achieving high-precision, robust, ubiquitous, and intelligent navigation and positioning in challenging scenarios.

Existing fusion frameworks can be broadly categorized into two main methods: filter-based methods (Chiang et al., 2019; Chiang et al., 2020; Li et al., 2021; Nguyen-Ngoc et al., 2023; Wang et al., 2023) and factor graph-based methods (He et al., 2023; Li et al., 2020; Liu et al., 2023). Among the filter-based methods, a representative example is FAST-LIO (Xu and Zhang, 2021). This method employs iterative extended Kalman filtering (IEKF) to achieve tightly coupled between LiDAR points and IMU data, demonstrating exceptional robustness in high-speed motion, strong noise, and cluttered environments. However, the linearization errors inherent in the filtering framework can degrade long-term accuracy. In the factor graphbased approaches, LIO-SAM utilizes IMU pre-integration to provide an initial estimate for LiDAR odometry (LO) optimization (Shan et al., 2020). This framework innovatively incorporates absolute GNSS observations as constraints to enhance positioning accuracy. A further improvement integrates visual information to achieve more precise real-time state estimation and map construction (Shan et al., 2021). However, the computational complexity of factor graph optimization (FGO) increases with the number of nodes, posing challenges to real-time performance. Additionally, in GNSS-denied

E-mail address: yzcong@sdu.edu.cn (Yangzi Cong).

<sup>\*</sup> Corresponding author.

environments, these systems remain susceptible to cumulative errors.

For GNSS Non-Line-Of-Sight (NLOS) correction, one of the most widely adopted approaches is 3D mapping-assisted (3DMA) GNSS positioning (Kbayer and Sahmoudi, 2018; Wang et al., 2013; Zhou, 2022). However, the effectiveness of this method is heavily reliant on both the accuracy of the 3D building model and the precision of the GNSS receiver's initial position estimate. In addition to 3DMA-based approaches, fisheye camera-assisted methods have also been explored (Kato et al., 2016; Sánchez et al., 2016). While these methods offer potential improvements in NLOS detection, their performance is highly sensitive to variations in lighting conditions, leading to significant degradation in low-light environments or adverse weather conditions.

Although significant progress has been made in the field of multi-source sensor fusion navigation, existing methods still need to be improved. In particular, there is a need to enhance sensor complementarity, measurement error suppression, and environmental adaptability to meet the demands for highprecision and robust navigation and positioning. To address these challenges, this study proposes a lightweight and highly flexible LiDAR/IMU/GNSS tightly coupled navigation framework. Inspired by the work of Wen (Wen et al., 2022), the framework introduces an innovative LiDAR-assisted GNSS NLOS detection and correction module. By leveraging LiDAR point clouds to construct real-time environmental geometric constraints, the system accurately detects NLOS signals. An error compensation model is developed to correct the contaminated GNSS observations based on the detection result. The quality-optimized GNSS raw observations are then integrated into the navigation solver, providing reliable global constraints for the system, which significantly enhances navigation accuracy and robustness in complex environments.

# 2. Methodology

## 2.1 Problem Description

The LiDAR/IMU/GNSS framework proposed in this study is implemented within the factor graph framework, as illustrated in Figure 1. The system's state vector can be expressed as follows:

$$\mathbf{x} = [\mathbf{q}^{\mathrm{T}}, \mathbf{v}^{\mathrm{T}}, \mathbf{p}^{\mathrm{T}}, \mathbf{b}^{\mathrm{T}}]^{\mathrm{T}} \tag{1}$$

where q denotes the attitude quaternion, v is the velocity vector, p is the position vector, and b is the bias of the IMU.

Based on the principle of FGO, the carrier position estimation problem can be formulated as a maximum a posteriori (MAP) probability estimation, expressed as follows:

$$\min_{\mathcal{X}} \left\{ \begin{aligned} & \left\| \left\| \mathbf{r}_{p} - \mathbf{H}_{p} \mathbf{X} \right\|^{2} + \sum_{k \in \mathbf{B}} \left\| \mathbf{d}_{ek}^{\mathbf{M}} \right\|_{\Sigma_{e}}^{2} + \sum_{k \in \mathbf{B}} \left\| \mathbf{d}_{pk}^{\mathbf{M}} \right\|_{\Sigma_{p}}^{2} \\ & + \sum_{k \in \mathbf{B}} \left\| \mathbf{r}_{\mathbf{B}}^{15 \times 1} \left( \hat{\mathbf{z}}_{b_{k+1}}^{b_{k}}, \mathbf{X} \right) \right\|_{\Sigma_{b}}^{2} + \sum \left\| \mathbf{r}_{\mathbf{DD}, \rho, \mathbf{r}, t}^{\mathbf{t}} \right\|_{\sigma_{p}}^{2} \end{aligned} \right\}$$
(2)

where  $\|r_p-H_pX\|^2$  is the a priori information,  $r_B\left(\hat{z}_{b_{k+1}}^{b_k},X\right)$  denotes the IMU measurement residuals,  $\Sigma_b$  denotes the IMU measurement covariance matrix,  $d_{ek}^M$  and  $d_{pk}^M$  denote the

LiDAR point-to-line residuals and point-to-plane residuals in the local coordinate system of the k-th frame of LiDAR in Map frame (M-frame),  $\Sigma_e$  and  $\Sigma_p$  denote the corresponding covariance matrices, respectively.  $r^s_{DD,\rho,r,t}$  denotes the residual of the pseudorange difference, and  $\sigma_\rho$  is the uncertainty of the pseudorange measurement, initially calculated based on the signal-to-noise ratio and elevation angle.

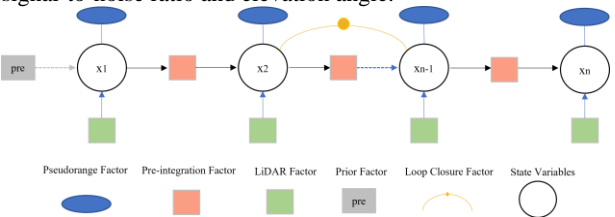


Figure 1. Factor graph model of LiDAR/INS/GNSS tightly coupled system.

## 2.2 LiDAR-Aided GNSS NLOS Satellite Detection

In areas with dense buildings and tree cover, GNSS signals are often subject to NLOS propagation, leading to increased observation errors and a significant degradation in positioning accuracy. To mitigate the impact of NLOS on the performance of GNSS/LIO fusion systems, this study proposes a novel GNSS NLOS error correction method based on LiDAR point clouds.

Specifically, point clouds accumulated from historical LiDAR scans form a three-dimensional map of the carrier's current environment, and the density of the LiDAR point clouds in the line-of-sight direction of the carrier and the satellite is then analysed to determine whether the satellite is obscured. For NLOS satellites, the possible reflection paths of the satellite in map are searched to correct for NLOS errors in GNSS pseudorange observations.

The correction process is divided into three main steps: detecting NLOS satellites, identifying NLOS reflection points, and correcting the NLOS error, which is shown in Figure 2. First, to detect NLOS satellites, the system uses consecutive multi-frame LiDAR point clouds to construct a local environmental map. The history keyframe poses are obtained from the previous sliding window optimization, so a more accurate local map can be constructed. And a kd-tree data structure is employed for efficient storage and management.

According to its azimuth angle  $\alpha_{r,t}$  and elevation angle  $\epsilon_{r,t}$ , combined with the carrier's initial position  $p_0 = \left(x_t^M, y_t^M, z_t^M\right)$ , ray-tracing is performed along the satellite signal propagation direction. In detail, starting from  $p_0$ , the carrier is moved incrementally along the satellite direction with a fixed step size  $\Delta d$ . The coordinates of the k-th sampling point can be calculated as:

$$\begin{cases} x_{t,k}^{M} = x_{t,k-1}^{M} + \Delta d \sin\left(\alpha_{r,t}\right) \cos\left(\epsilon_{r,t}\right) \\ y_{t,k}^{M} = y_{t,k-1}^{M} + \Delta d \cos\left(\alpha_{r,t}\right) \cos\left(\epsilon_{r,t}\right) \\ z_{t,k}^{M} = z_{t,k-1}^{M} + \Delta d \sin\left(\epsilon_{r,t}\right) \end{cases}$$
(3)

"Mobile Mapping for Autonomous Systems and Spatial Intelligence", 20–22 June 2025, Xiamen, China

After obtaining the new position, the LiDAR points in the neighbouring area will be searched by kd-tree, the number of which is noted as  $N_k$ . If  $N_k\!>\!N_{\text{lim}}$ , this indicates that there is an obstruction in the propagation path of the GNSS signal, then the satellite is considered as a NLOS satellite; otherwise there is no NLOS occurrence until the distance moved exceeds the maximum set distance D.

Secondly, if the satellite is identified as an NLOS satellite, the NLOS errors present in the GNSS signal must be corrected for use in the multi-source sensor information fusion. For signal reflection, the path usually consists of two parts, the first part is from the GNSS satellite to the reflection point and the second part is the signal transmission from the reflection point to the antenna. Therefore, finding the possible reflection point of the reflected signal is a key problem for NLOS errors. Generally, the reflected part of the signal should have the same elevation angle as the expected direct signal. Accordingly, we will look for potential reflection points in the carrier's local map.

For NLOS satellites, the current local point cloud map is divided into U divisions at equal intervals according to a fixed  $\alpha_{res}$  angle, where U=360/ $\alpha_{res}$ . For each area, we search for the presence of occlusion along the direction of elevation angle  $\epsilon_{r,t}$  following the method of searching NLOS above. If it exists, the occlusion point is identified in the direction of the height angle  $\epsilon_{r,t}$  in the occlusion point cloud and the point  $\left(x_{t,k}^M,y_{t,k}^M,z_{t,k}^M\right)$  is stored in the set Q. Each area is then traversed to find all potential reflection points.

Finally, the distance from the GNSS antenna for each candidate reflection point in the set Q is calculated. The reflection point  $P_{t,ref}^{M}$  with the smallest distance from the current carrier position is taken as the reflection point (Hsu, 2018) and this distance is denoted as R. And the NLOS correction quantity  $\Delta\delta_{r,t}^{L}$  is as follows:

$$\Delta \delta_{r,t}^{M} = \operatorname{Rsec}(\varepsilon_{r,t}) + \operatorname{Rsec}(\varepsilon_{r,t}) \cos(2\varepsilon_{r,t})$$
 (4)

By incorporating the NLOS correction into the original GNSS observations, the impact of NLOS propagation on positioning accuracy can be effectively mitigated. Figure 3 illustrates the complete process of the LiDAR-based GNSS NLOS error correction algorithm.

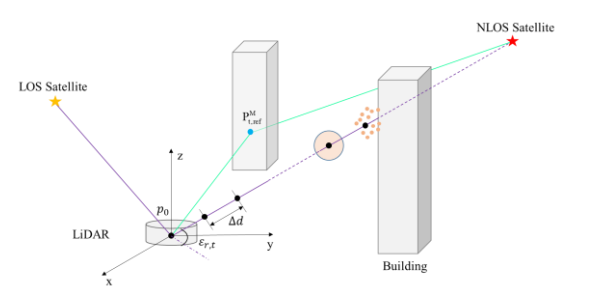


Figure 2. The NLOS detection and correction.

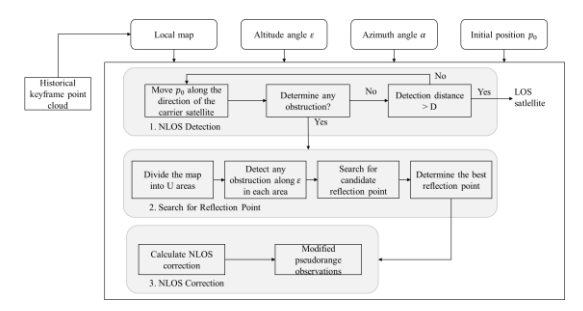


Figure 3. LiDAR assisted GNSS correction of NLOS error process.

# 2.3 LiDAR Odometry Factor

Based on the roughness, the feature points can be classified into edge points and planar points, and the residual equations of the two types of feature point clouds are constructed separately to obtain the final LiDAR cost function. The residual construction of the two types of LiDAR feature points is shown in Figure 4.

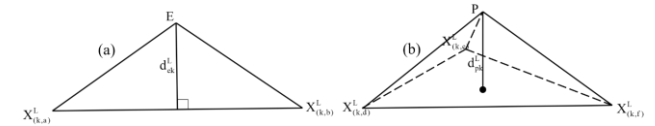


Figure 4. Residual construction for LiDAR (a) edge points and (b) planar points.

Let point E be a corner point in the LiDAR k+1-th frame point cloud with coordinates  $X_{(k+1,E)}^M$ , and its corresponding two corner points in the k-th frame point cloud with coordinates  $X_{(k,a)}^M$  and  $X_{(k,b)}^M$ , then the corner point feature residuals can be expressed by the distance from point  $X_{(k+1,o)}^M$  to the line where  $X_{(k,a)}^M$  and  $X_{(k,b)}^M$  points are located by the following formula:

$$d_{ek}^{M} = \frac{\left| \left( X_{(k+1,E)}^{M} - X_{(k,a)}^{M} \right) \times \left( X_{(k+1,o)}^{M} - X_{(k,b)}^{M} \right) \right|}{\left| X_{(k,a)}^{M} - X_{(k,b)}^{M} \right|}$$
(5)

Similarly, let point O be a plane point in the LiDAR k+1-th frame point cloud with coordinates  $X^M_{(k+1,P)}$ , and its corresponding plane point coordinates in the k-th frame point cloud are  $X^M_{(k,c)}$ ,  $X^M_{(k,d)}$  and  $X^M_{(k,f)}$  then the planar point feature residuals can be expressed by the point-to-plane distances from  $X^M_{(k+1,P)}$  to the planes where the points  $X^M_{(k,c)}$ ,  $X^M_{(k,d)}$  and  $X^M_{(k,f)}$  are located as the following equation:

$$d_{pk}^{M} = \frac{\left| \left( X_{(k+1,O)}^{M} - X_{(k,d)}^{M} \right) \cdot \left( \left( X_{(k,c)}^{M} - X_{(k,d)}^{M} \right) \times \left( X_{(k,c)}^{M} - X_{(k,f)}^{M} \right) \right) \right|}{\left| \left( X_{(k,c)}^{M} - X_{(k,d)}^{M} \right) \times \left( X_{(k,c)}^{M} - X_{(k,f)}^{M} \right) \right|}$$
(6)

# 2.4 Loop Closure Factor

In this study, we present a robust loop closure detection method that integrates multimodal information, effectively addressing the loop closure detection challenges in SLAM systems within complex environments. The method combines geometric constraints with global descriptor techniques. For geometric

matching, a map-to-map ICP point cloud matching strategy is employed, replacing the traditional frame-to-frame approach. This significantly enhances the accuracy and robustness of point cloud alignment by aggregating point clouds from consecutive frames near the current frame to construct a local sub-map. To address geometric loop closure failures caused by error accumulation in large-scale scenes, a global descriptorbased context scan loopback detection method is utilized. It projects the 3D point cloud onto a 2D polar coordinate space and constructs a height feature matrix with rotational invariance. As shown in Figure 5, the perceptual space is discretized into feature units with clear physical meaning, using n radial concentric rings and m axial rays. Each unit stores the maximum height value, preserving key geometric features while achieving data compression. This feature representation is robust to changes in viewing angle, and loop closure detection is accomplished through feature matrix similarity metrics, thereby mitigating the impact of cumulative errors.

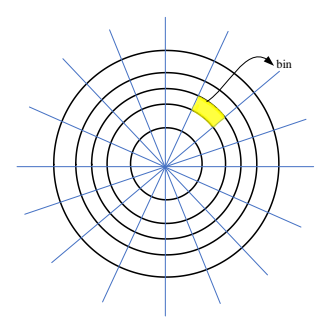


Figure 5. Constructing the surrounding environment as a global descriptor based on context scanning matching loop closure detection.

# 2.5 Double-Difference Pseudorange Factor

The GNSS pseudorange observation P is expressed as:

$$P = \rho + cdt_r - cdt^s + T + I + H_r - H^s + \varepsilon_P$$
 (7)

where,  $\rho$  is the Euclidean distance from the GNSS receiver to the satellite, c is the propagation speed of light in vacuum,  $dt_r$  and  $dt^s$  the clock difference of the receiver and satellite, respectively. T and I are the tropospheric and ionospheric delays,  $H_r$  and  $H^s$  are the pseudorange hardware delays of the receiver and the satellite, respectively, and  $\epsilon_P$  denotes the measurement noise of the pseudorange.

To eliminate the effects of clock errors and atmospheric delays on pseudorange observations, the pseudorange double-difference processing is performed between stations and satellites. The residual equation for pseudorange differencing is given as follows:

$$r_{\text{DD,o,r,t}}^{s} = \left(P_{\text{r,t}}^{s} - P_{\text{e,t}}^{s}\right) - \left(P_{\text{r,t}}^{w} - P_{\text{e,t}}^{w}\right) - \left(\rho_{\text{r,t}}^{s} - \rho_{\text{e,t}}^{s}\right) - \left(\rho_{\text{r,t}}^{w} - \rho_{\text{e,t}}^{w}\right)$$
(8)

where  $r_{DD,p,r,t}^s$  denotes the residual of pseudorange differencing, subscripts r and e denote rover and reference stations, and superscripts w and s are the reference satellite and other satellites, respectively.

## 2.6 IMU pre-integration factor

Typically, the sampling frequency of the IMU is higher than that of the LiDAR. Therefore, the IMU's integrated values over a given time period can be used to provide an a priori position estimate for LiDAR at the next time step, facilitating faster convergence during LiDAR matching. However, since the IMU zero bias changes with each iteration, re-integrating based on the post-iteration values at every step would be time-consuming. To address this, we use IMU pre-integration and the residuals of the IMU pre-integration factors are expressed as follows:

$$r_{B}^{\text{15x1}}\!\!\left(\!\hat{z}_{b_{k+1}}^{b_{k}}, X\!\right) \!=\! \begin{bmatrix} \delta\alpha_{b_{k+1}}^{b_{k}} \\ \delta\theta_{b_{k+1}}^{b_{k}} \\ \delta\beta_{b_{k+1}}^{b_{k}} \\ \delta\nabla_{\delta\epsilon}^{b} \end{bmatrix} \!=\! \begin{bmatrix} R_{w}^{b_{k}}\!\left(p_{b_{k+1}}^{w} \!-\! p_{b_{k}}^{w} \!-\! v_{b_{k}}^{w} \!\Delta t_{k} \!+\! \frac{1}{2}g^{w} \!\Delta t_{k}^{2}\right) \!-\! \alpha_{b_{k+1}}^{b_{k}} \\ 2\!\left[\left(\gamma_{b_{k+1}}^{b_{k}}\right)^{\!-\!1} \otimes q_{b_{k}}^{w^{-}} \otimes q_{b_{k+1}}^{w}\right] \\ R_{w}^{b_{k}}\!\left(v_{b_{k+1}}^{w} \!-\! v_{b_{k}}^{w} \!+\! g^{w} \!\Delta t_{k}\right) \!-\! \beta_{b_{k+1}}^{b_{k}} \\ \nabla_{b_{k+1}}^{b} \!-\! \nabla_{b_{k}}^{b} \\ \varepsilon_{b_{k+1}}^{b} \!-\! \varepsilon_{b_{k}}^{b} \end{bmatrix}$$

### 3. Experiment and Results

# 3.1 Performance of LiDAR-Assisted GNSS NLOS Detection

To evaluate the effectiveness of the proposed method, experiments were conducted using a multi-sensor data acquisition platform. The platform comprises a multi-frequency, multi-mode high-precision Septentrio receiver, a VLP-16 LiDAR, a high-resolution RGB camera, a HGuidei300 IMU, and a high-precision time synchronization board. All sensors are hardware-synchronized. The platform is shown in Figure 6. The results from the bidirectional smoothed commercial Inertial Explorer (IE) RTK/INS integrated solutions were used as the reference truth. The experimental data were collected at the School of Space Science and Technology, Shandong University, with two sets of experiments conducted: one on the internal courtyard (denoted as SDU1) and the other on the exterior (SDU2) of the building. During the experiments, the data collection platform was consistently surrounded by buildings or tall trees, which led to frequent NLOS conditions for GNSS.



Figure 6. Data collection platform.

Figure 7 (a) visualizes the LiDAR point cloud map and the geometric distribution of the satellites at an echo in the SDU1. At this moment, the system observed a total of 10 satellites, 9 of which were line-of-sight (LOS) satellites indicated by white circles. Only the PRN 4 satellite (marked in red) was identified as having NLOS propagation. The polar plot in Figure 7(b) further illustrates the elevation angle and azimuth angle of each satellite. Notably, despite the significantly lower elevation angles of satellites PRN 27 (25.54 °) and 61 (29.46 °) compared to PRN 4 (38.72 °), no signal occlusion occurs. This is because the azimuths of PRN 27 and 61 are positioned at 175.89 ° and

"Mobile Mapping for Autonomous Systems and Spatial Intelligence", 20–22 June 2025, Xiamen, China

185.71 ° (near due south), and the carrier is further away from the south wall at this time. In contrast, PRN 4 is located at an azimuth of 297.23 ° (northwest), and its signal propagation path is obstructed by nearby buildings. This obstruction is calculated to require an NLOS correction of 13.99 m. This observation confirms that satellite occlusion in an urban canyon environment is not only dependent on elevation angle, but is also closely related to the spatial distribution of surrounding buildings.

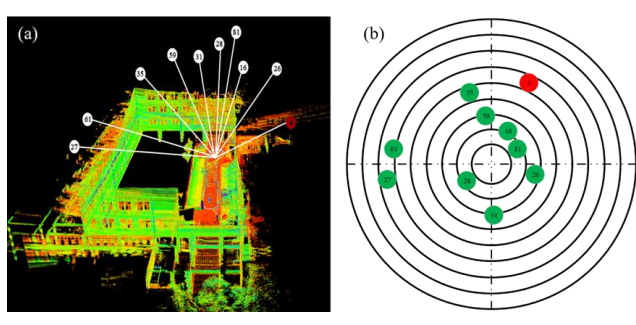


Figure 7. (a) The geometric relationship between the satellites observed at a certain moment in SDU1 and the surrounding buildings, and (b) the corresponding elevation and azimuth angles of the satellite.

Figure 8 shows the GNSS observation characteristics of two datasets. In the SDU1, the system cumulatively observed 7 GPS satellites, 5 GALILEO satellites, and 1 BDS satellite, with approximately 8 satellites maintaining stable tracking. The results of LiDAR-assisted NLOS detection showed that the NLOS occurred in GPS PRN 4 and 27 satellites. Notably, although PRN 27 is located in the low-elevation region to the south of the carrier (at an elevation angle of about 25°), the proximity of the carrier to the south wall at the end period of the experiment caused this satellite's signal to switch to NLOS. In the SDU2 experiment, the system observed a total of 8 GPS satellites and 6 GALILEO satellites, with 7 satellites maintaining stable tracking. The detection results indicated that intermittent NLOS phenomena are present in GPS PRN 4 and 16, and GALILEO PRN 25 satellites. The analysis reveals that the reasons for the NLOS generation of satellites PRN 16 and 25 are similar to that of PRN 27 in the SDU1 experiment, both showing a strong correlation with the spatial relationship between the satellites, the carrier and the surrounding buildings.

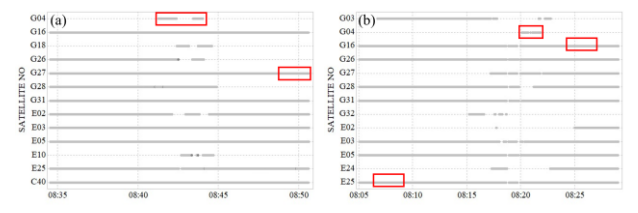


Figure 8. Observable satellites of (a) SDU1 and (b) SDU2 and the NLOS periods. The grey dots represent observable satellites, and the red rectangle parts represent NLOS detected by proposed method.

Figure 9, Figure 10 and Table 1 demonstrate the position error of the LiDAR/INS/GNSS integration navigation system with and without NLOS correction (denoted as LIGON and LIGO w/o N). In the SDU1, the system with NLOS correction achieves a horizontal positioning accuracy of 0.694 m and a 3D

positioning accuracy of 1.162 m, an improvement of 14.63% and 14.91% respectively over the uncorrected system. It can be observed that the uncorrected system has a maximum position error of approximately -1.4 m in the E direction, while the corrected system effectively limits this error. Despite the relatively low percentage of NLOS satellites in the SDU1, the correction algorithm consistently yields a stable improvement of 14.28% in U direction positioning accuracy. In the SDU2, the horizonotal positioning accuracy improved by 17.45% in LIGON system, with the most significant enhancement observed in the U direction, where the U direction error was reduced from 1.571m to 1.259m. The experimental results demonstrate that the NLOS correction method significantly improves the performance of the integration navigation system, particularly for vertical positioning, which is more vulnerable to GNSS signal disruptions. Additionally, the method effectively suppresses sudden position bias in the U direction.

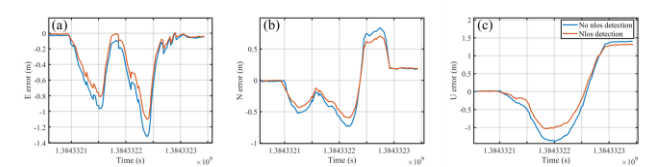


Figure 9. Error sequences of the LIGON and LIGO w/o N in the SDU1.

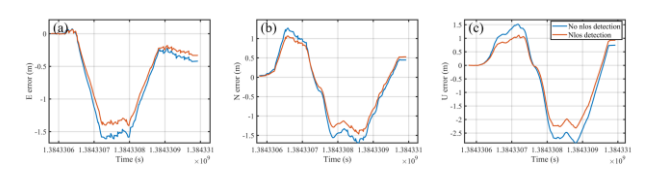


Figure 10. Error sequences of the LIGON and LIGO w/o N in the SDU2.

Dataset	Scheme	Е	N	U
SDU1	LIGO w/o N	0.528	0.451	0.932
	LIGON	0.446	0.385	0.797
CDUA	LIGO w/o N	0.922	0.992	1.571
SDU2	LIGON	0.782	0.852	1.259

Table 1. The accuracy statistics of the LIGON and LIGO w/o N in the SDU1 and SDU2 datasets (unit: m)

## 3.2 The Comparative Experiments

In order to more fully validate the performance of the LiDAR/INS/GNSS system with LiDAR-assisted NLOS correction, a comparative analysis with other combined navigation schemes was conducted. The experimental data were collected using a data acquisition platform at the Shandong University campus for two datasets: the open scene dataset (SDU3) and the semi-open scene (SDU4) dataset. The comparison schemes are as follows:

- (1) LIO: The tightly coupled system of LiDAR and IMU.
- (2) **LIO-RTD**: The LiDAR/INS system is loosely coupled with double-difference pseudorange positioning results.

"Mobile Mapping for Autonomous Systems and Spatial Intelligence", 20–22 June 2025, Xiamen, China

(3) **LIO-RTK**: The loosely coupled integration between LiDAR/INS and carrier phase differential positioning results.

(4) **LIGO-N**: The tightly coupled integration between LiDAR/INS and raw differential pseudorange measurements, fused with proposed NLOS detection and correction (proposed).

Figure 11 illustrates the scenarios and reference truth in SDU3, which shows a more open environment where the surrounding buildings are away from the platform and there is no severe signal occlusion. The experiment utilizes the GPS, Galileo, and BDS observations with an elevation angle of more than 15°. Figure 12 shows that the average number of visible satellites is 17.3 and the average DOP value is 2.4. It indicates a favourable satellite geometry, providing strong a priori conditions for the accurate GNSS positioning.



Figure 11. The SDU3 trajectory and scenarios.

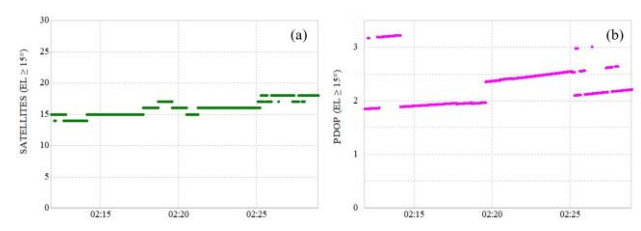


Figure 12. (a) The number of observable satellites and (b) PDOP in SDU3.

Figure 13 and Figure 14 are trajectories and position error sequences of different navigation schemes in the SDU3. The corresponding RMSE results are summarized in Table 1.The error sequences and trajectory results show that the trajectory of the LIO deviates significantly from the reference trajectory, especially in the U direction. Furthermore, this deviation increases with the accumulation of sensor errors and is partially suppressed by the introduction of a loop closure factor when the trajectory closes. The RMSE of the 3D position is 20.396 m.

In contrast, the trajectories of the LIO-RTD and LIGO-N schemes, which incorporate GNSS information, are noticeably closer to the reference truth. Partial view shows that the trajectories of LIO-RTD and LIGO-N overlap due to no NLOS conditions in the open scene. The error for both schemes is very small, within 1 m in all directions. Accuracy in the E, N and U directions is significantly improved compared to LIO, especially in the U direction where the error is significantly reduced. This demonstrates that the LiDAR/INS scheme achieves higher positioning accuracy when assisted by GNSS global information, and there is little difference between loosely and tightly coupled with GNSS in open scene.

In the open environment, due to the sufficient number of observable satellites, the RTK achieves the superior positioning performance. Therefore, the cumulative error of the LIO-RTK system integrated with RTK is effectively suppressed and its RMSE is less than 0.2 m the horizontal direction. The LIO-RTK provides the highest positioning accuracy, with horizontal and vertical position RMSE of 0.241 m and 0.701 m respectively.

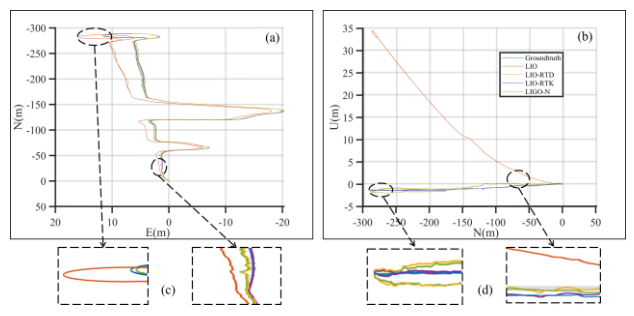


Figure 13. Different solutions in SDU3 include (a) horizontal and (b) vertical trajectories, (c) and (d) are local trajectories.

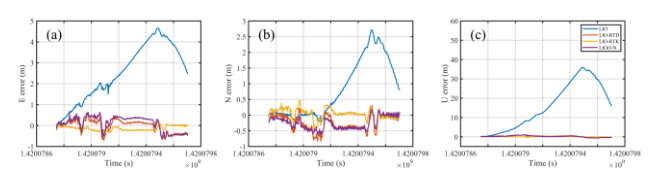


Figure 14. Error sequences of different coupled navigation schemes in directions (a) E, (b) N and (c) U in SDU3.

The total duration of the SDU4 experiment is about 8 minutes. Compared to SDU3, the SDU4 dataset is a more complex environment with trees and buildings on both sides of the road and pedestrian activity. Figure 15 shows the test trajectory with surrounding scenario, while Figure 16 illustrates the variation in the number of observable satellites and the PDOP.

In SDU4, the number of observable satellites drops dramatically, with an average of only 5.8 satellites visible. In addition, during the period from 8:40 to 8:41, there were fewer than 4 observable satellites in some epochs due to the experimental platform passing through an area obstructed by buildings. This further increases the uncertainty of the positioning and causes difficulties for GNSS positioning. Throughout the entire experiment, the average PDOP is 3.7. However, during the periods of 8:36-8:37 and 8:40-8:41, the PDOP value increases significantly. Notably, during 8:40-8:41, the PDOP value exceeds 9 due to building obstructions, indicating a deterioration in satellite geometry and presenting greater challenges for GNSS positioning.



Figure 15. The SDU4 trajectory with scenarios.

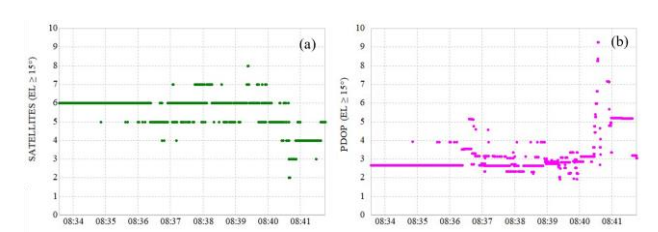


Figure 16. (a) The number of observable satellites and (b) PDOP in SDU4.

Figure 17 and Figure 18 show the trajectories and error sequences for the SDU4 dataset. Due to the more complex environment and poor quality of GNSS satellite observations, the positioning accuracies of LIO-RTD, LIGO-N, and LIO-RTK are degraded compared to the open SDU3. As with SDU3, the LIO trajectories deviate significantly from the reference truth. In contrast, the error between the trajectories of the integration systems coupled with GNSS information and the true trajectory is smaller. The local image reveals that the LIGO-N trajectory is closer to the reference truth trajectory than that of LIO-RTD. When the number of observable satellites is less than 4, GNSS cannot complete the solution, so LIO-RTD is not constrained by valid global information in some echoes.

On the contrary, LIGO-N is still able to reduce the systematic error using the pseudorange difference information in this case. In addition, by conducting NLOS detection and correction, the errors in GNSS pseudorange observations are eliminated and LIGO-N performs better than the LIO-RTD. Overall, the 3D positioning accuracy of LIGO-N is improved by 32.57% compared to LIO-RTD, with the most significant improvement observed in the U direction, reducing the error from 1.747 m to 1.161 m. However, LiDAR/INS/RTK still achieves the highest positioning accuracy, owing to the carrier-based differential positioning mode of GNSS RTK.

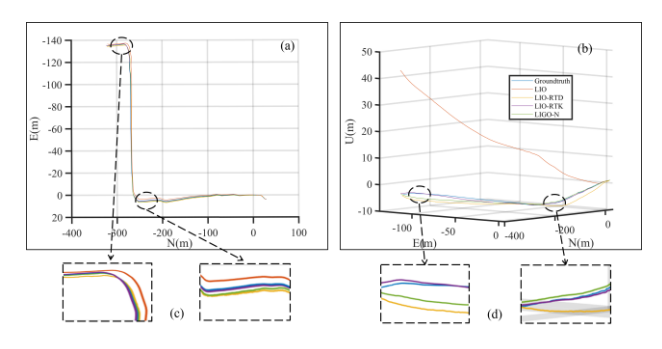


Figure 17. Different solutions in SDU4 include (a) horizontal and (b) vertical trajectories, (c) and (d) are local trajectories.

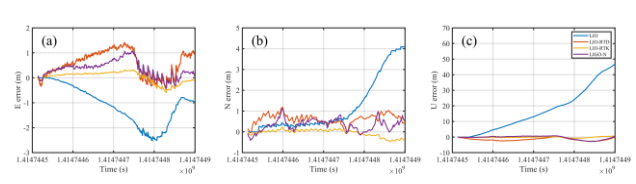


Figure 18. Error sequences of different coupled navigation schemes in directions (a) E, (b) N and (c) U in SDU4.

Dataset	Solution	Е	N	U
SDU3	LIO	2.919	1.263	20.396
	LIO-RTD	0.353	0.331	0.934
	LIO-RTK	0.173	0.168	0.701
	LIGO-N	0.316	0.343	0.997
SDU4	LIO	1.401	1.814	22.733
	LIO-RTD	0.819	0.772	1.747
	LIGO- RTK	0.330	0.274	0.840
	LIGO-N	0.574	0.535	1.161

Table 2. Statistics on the accuracy of navigation results of different solutions (unit: m)

# 4. Conclusions

In this study, a tightly coupled LiDAR/IMU/GNSS navigation framework is proposed, along with the construction of a LiDAR/INS/GNSS FGO model. Additionally, a LiDARassisted GNSS NLOS satellite detection method is introduced. Experimental results validate the effectiveness of the method and assess the positioning accuracy of the framework in various scenarios. The results show that in environments prone to NLOS, the proposed NLOS detection and correction method effectively compensates for GNSS errors, leading to an overall improvement in positioning accuracy for the LiDAR/INS/GNSS integrated navigation system by approximately 16.15%. In open environments, the framework does not exhibit significant advantages, but in complex environments, the NLOS-corrected combined navigation scheme notably enhances positioning accuracy by 32.57%. It also ensures continuous GNSS information constraints on the system, thereby improving navigation stability and robustness compared to the system without NLOS correction.

### Acknowledgements

This research was jointly funded by the Natural Science Foundation of Shandong Province (No. ZR2024QD246), Open Research Fund Program of LIESMARS (Grant No. 24A06) and State-funded postdoctoral researcher program (No. GZC20231482).

### References

Chiang, K. W., Tsai, G. J., Chang, H., et al., 2019. Seamless navigation and mapping using an INS/GNSS/grid-based SLAM

- semi-tightly coupled integration scheme. Information Fusion, 50, 181-196. https://doi.org/10.1016/j.inffus.2019.01.004.
- Chiang, K. W., Tsai, G. J., Chu, H. J., et al., 2020. Performance enhancement of INS/GNSS/Refreshed-SLAM integration for acceptable lane-level navigation accuracy. IEEE Transactions on Vehicular Technology, 69(3), 2463-2476. doi: 10.1109/TVT.2020.2966765.
- He, X., Pan, S., Gao, W., et al., 2022. LiDAR-Inertial-GNSS fusion positioning system in urban environment: Local accurate registration and global drift-free. Remote Sensing, 14(9), 2104. https://doi.org/10.3390/rs14092104.
- Hsu, LT., 2018. Analysis and modeling GPS NLOS effect in highly urbanized area. GPS Solut 22, 7. https://doi.org/10.1007/s10291-017-0667-9.
- Kato, S., Kitamura, M., Suzuki, T., Amano, Y., 2016. NLOS satellite detection using a fish-eye camera for improving GNSS positioning accuracy in urban areas. Journal of Robotics and Mechatronics, 28(1), 31-39. https://doi.org/10.20965/jrm.2016.p0031.
- Kbayer, N., Sahmoudi, M., 2018. Performances analysis of GNSS NLOS bias correction in urban environment using a three-dimensional city model and GNSS simulator. IEEE Transactions on Aerospace and Electronic Systems, 54(4), 1799-1814. doi: 10.1109/TAES.2018.2801658.
- Kuutti, S., Fallah, S., Katsaros, K., Dianati, M., Mccullough, F., Mouzakitis, A., 2018. A Survey of the State-of-the-Art Localization Techniques and Their Potentials for Autonomous Vehicle Applications. IEEE Internet of Things Journal, 5(2), 829-846. doi: 10.1109/JIOT.2018.2812300.
- Garg, S.C., Morrow, L.D., Mamen, R., 1978. Strapdown navigation technology: A literature survey. Journal of Guidance and Control, 1(3), 161-172.
- Li, X., Wang, H., Li, S., et al., 2021. GIL: A tightly coupled GNSS PPP/INS/LiDAR method for precise vehicle navigation. Satellite Navigation, 2, 1-17. https://doi.org/10.1186/s43020-021-00056-w.
- Li, X., Yu, H., Wang, X., et al., 2023. FGO-GIL: Factor graph optimization-based GNSS RTK/INS/LiDAR tightly coupled integration for precise and continuous navigation. IEEE Sensors Journal, 23(13), 14534-14548. doi: 10.1109/JSEN.2023.3278723.
- Liu, X., Wen, W., Hsu, L.T., 2023. GLIO: Tightly-coupled GNSS/LiDAR/IMU integration for continuous and drift-free state estimation of intelligent vehicles in urban areas. IEEE Transactions on Intelligent Vehicles, 9(1), 1412-1422. doi: 10.1109/TIV.2023.3323648.
- Nguyen-Ngoc, T. T., Phi, T. D., Phan-Nguyen, P. Q., et al., 2023. Tightly-coupled GPS/INS/Lidar Integration for Road Vehicles. 2023 International Symposium on Electrical and Electronics Engineering (ISEE), 156-160. doi: 10.1109/ISEE59483.2023.10299860.
- Pinana-Diaz, C., Toledo-Moreo, R., Betaille, D., Gomez-Skarmeta, A.F., 2011. GPS multipath detection and exclusion with elevation-enhanced maps. Intelligent Transportation

- Systems (ITSC), 14th International IEEE Conference on, 2011, 19-24. IEEE. doi: 10.1109/ITSC.2011.6083042.
- Sánchez, J. S., Gerhmann, A., Thevenon, P., Brocard, P., Afia, A. B., Julien, O., 2016. Use of a FishEye camera for GNSS NLOS exclusion and characterization in urban environments. ION ITM 2016, International Technical Meeting. ION. https://doi.org/10.33012/2016.13404.
- Shan, T., Englot, B., 2018. Lego-loam: Lightweight and ground-optimized lidar odometry and mapping on variable terrain. 2018 IEEE/RSJ International Conference on Intelligent Robots and Systems (IROS), 4758-4765. doi: 10.1109/IROS.2018.8594299.
- Shan, T., Englot, B., Meyers, D., et al., 2020. Lio-sam: Tightly-coupled lidar inertial odometry via smoothing and mapping. In: 2020 IEEE/RSJ International Conference on Intelligent Robots and Systems (IROS), IEEE, 5135-5142. doi: 10.1109/IROS45743.2020.9341176.
- Shan, T., Englot, B., Ratti, C., et al., 2021. Lvi-sam: Tightly-coupled lidar-visual-inertial odometry via smoothing and mapping. In: 2021 IEEE International Conference on Robotics and Automation (ICRA), IEEE, 5692-5698. doi: 10.1109/ICRA48506.2021.9561996.
- Smith, J., 2000. Remote sensing to predict volcano outbursts. *Int. Arch. Photogramm. Remote Sens. Spatial Inf. Sci.*, XXVII-B1, 456-469.
- Vivacqua, R., Vassallo, R., Martins, F., 2017. A low-cost sensors approach for accurate vehicle localization and autonomous driving application. Sensors, 17(10), 2359. https://doi.org/10.3390/s17102359.
- Wang, L., Groves, P. D., Ziebart, M. K., 2013. GNSS shadow matching: Improving urban positioning accuracy using a 3D city model with optimized visibility scoring scheme. Navigation, 60(3), 195-207. https://doi.org/10.1002/navi.38.
- Wang, M., Cong, M., Liu, D., et al., 2023. Tightly coupled IMU-Laser-RTK odometry algorithm for underground multi-layer and large-scale environment. Industrial Robot: the international journal of robotics research and application, 50(6), 878-887. https://doi.org/10.1108/IR-11-2022-0281.
- Wen, W. W., Hsu, L.-T., 2022. 3D LiDAR Aided GNSS NLOS Mitigation in Urban Canyons. IEEE Transactions on Intelligent Transportation Systems, 23(10), 18224-18236. doi: 10.1109/TITS.2022.3167710. doi: 10.1109/TITS.2022.3167710.
- Xu, W., Zhang, F., 2021. Fast-lio: A fast, robust lidar-inertial odometry package by tightly-coupled iterated kalman filter. IEEE Robotics and Automation Letters, 6(2), 3317-3324. doi: 10.1109/LRA.2021.3064227.
- Yang, F., Jie, B., Song, H., 2023. LIEO-SAM-Iris: Tightly-coupled Lidar Inertial Encoder Odometry via Smoothing and Mapping based on Iris loop closure. Proceedings of the 2023 9th International Conference on Computing and Artificial Intelligence, 759-764. https://doi.org/10.1145/3594315.3594402.

- Yang, Y., Gao, W., Guo, S., et al., 2019. Introduction to BeiDou- 3 navigation satellite system. Navigation, 66(1), 7-18. https://doi.org/10.1002/navi.291.
- Yang, Y., Li, J., Xu, J., et al., 2011. Contribution of the Compass satellite navigation system to global PNT users. Chin. Sci. Bull., 56, 2813–2819. https://doi.org/10.1007/s11434-011-4627-4.
- Zhang, J., Singh, S., 2014. LOAM: Lidar odometry and mapping in real-time. Robotics: Science and Systems, 2(9), 1-9.
- Zhang, J., Singh, S., 2017. Low-drift and real-time lidar odometry and mapping. Autonomous Robots, 41, 401-416. https://doi.org/10.1007/s10514-016-9548-2.
- Zhou, J., 2022. A review of LiDAR sensor technologies for perception in automated driving. Academic Journal of Science and Technology, 3(3), 255-261. doi: 10.1109/MITS.2019.2907630.